

A vertical slice frontogenesis test case for compressible nonhydrostatic dynamical cores of atmospheric models

Hiroe Yamazaki¹ and Colin J. Cotter^{*,1}

¹*Department of Mathematics, Imperial College London, UK*

^{*}*Correspondence to: colin.cotter@imperial.ac.uk*

January 17, 2025

Abstract

A new test case is presented for evaluating the compressible dynamical cores of the atmospheric models. The test case is based on a compressible vertical slice model that can be obtained by simple modification of a standard three dimensional compressible dynamical core. On the one hand, an advantage of the test case is that is quasi-2D, so it can be run quickly on a standard workstation, enabling rapid experimentation with numerical schemes and discretisation choices. On the other hand, the test case exhibits frontogenesis, a challenging regime for numerical discretisations which usually only arises in 3D model configurations for the compressible case. Numerical results of the test case using an implicit time-stepping method with a compatible finite element discretisation are presented as a reference solution. An example comparison between advective and vector-invariant forms for the advective nonlinearity in the velocity equation demonstrates one possible use of the scheme. The comparison shows a Hollingsworth-like instability when the vector invariant form is used.

keywords: frontogenesis; vertical slice; numerical weather prediction; model intercomparison

1 Introduction

Standardised test cases on hierarchies of models are a crucial element of atmospheric model dynamical core development. They are useful for code verification (checking that the code is a correct implementation of the mathematics), evaluation of the quality of discretisation choices (considering e.g. conservation properties, numerical dissipation and dispersion effects, etc.), benchmarking of computational speed and parallel scalability of models, and general intercomparison of models between modelling groups (Williamson et al., 1992; Galewsky et al., 2004; Läuter et al., 2005; Ullrich et al., 2015, 2012; Hall et al., 2016; Ullrich et al., 2017; Zarzycki et al., 2019).

Ideally, we would like to use testcases to develop confidence that the numerical solutions are converging to the true solution, but error calculations require a known exact solution. Exact solutions of the nonlinear equations are hard to find, especially solutions that are relevant to specific types of atmospheric flow. As an alternative, Cullen (2007) proposed to consider asymptotic limits (such as the quasigeostrophic or semigeostrophic limit), demonstrating convergence in the asymptotic limit to numerical solutions of the limit equation where the error is more under control.

Here we focus on the vertical slice Eady problem, which is important because it demonstrates the ability to simulate the geostrophic flows which are the basis of extratropical weather. In the incompressible Boussinesq case, the Euler solutions can be shown formally to converge to the solutions of the simpler semi-geostrophic system as a scaling parameter tends to zero. The latter solutions are discontinuous, and can be rigorously computed to any desired accuracy by optimal transport methods (Cullen, 2006;

Egan et al., 2022; Benamou et al., 2024; Lavier, 2024). They thus provide a challenging test for numerical methods for the Euler equations. Further, considering Euler, any solution will require regularisation, and Nakamura (1994) showed strong sensitivity to the choice of regularisation. The semigeostrophic limit solution is well defined, and conserves energy, with no need for regularisation. Hence, it can be argued that the correct limiting solution for Euler should have minimal numerical regularisation (explicit or implicit). For the incompressible vertical slice Eady model in the semigeostrophic limit, the asymptotic limit programme was pursued in Visram et al. (2014); Yamazaki et al. (2017).

The incompressible Boussinesq equations are not an ideal test for atmospheric models as they are not a good approximation to the compressible Euler equations, which are used in production atmospheric models, in problems with a significant vertical extent. There is thus a strong desire to reformulate the Eady test case for the compressible equations.

In this paper we present a compressible vertical slice model with initial conditions and parameter settings that lead to a frontogenesis lifecycle similar to the solutions considered in the incompressible case, and we offer this to the modelling community as an additional tool in their evaluation and intercomparison of atmosphere models.

The paper is structured as follows. Section 2 presents the full details of the new frontogenesis test case of compressible flow, including formation of the compressible Eady problem, settings of the frontogenesis experiment and the initial conditions. In Section 3, we apply the test case to an example model using an implicit time-stepping method with a compatible finite element discretisation, in order to provide a reference solution for other models of different numerical schemes. To evaluate the validity and reliability of the new test case, the results are compared to the solutions from the incompressible Euler–Boussinesq Eady models. A summary and outlook is provided in Section 4.

2 Test case description

2.1 Governing equations

In this section, we describe the model equations that are employed for the new vertical slice test case for compressible models. In the incompressible case, a 3D Eady problem can be solved using 2D computation by assuming that all variables are independent of y , except for temperature which has a time independent linear dependency on y , necessary to support the baroclinic instability that leads to frontogenesis. When compressibility is introduced, it is no longer possible to find similar quasi-2D solutions of the 3D model. We can only introduce *ad hoc* terms (motivated by the effects of a y -direction temperature gradient) to produce baroclinic instability. This was attempted in Cullen (2008), but unfortunately the proposed modifications did not have a conserved energy or potential vorticity, which are crucial in sustaining baroclinic instability towards frontogenesis. The question of how to build vertical slice models with conserved energy and potential vorticity was addressed by Cotter and Holm (2013), who identified the variational structure underpinning the incompressible vertical slice model. This structure establishes energy and potential vorticity conservation from within the vertical slice setting without needing to refer to the underlying 3D model. Then, other models that also conserve energy and potential vorticity can be derived by choosing a different Lagrangian (kinetic energy minus potential energy). Cotter and Cullen (2019) showed that the potential vorticity conservation in these models arises from a special form of particle relabelling symmetry in the slice geometry that incorporates the velocity in the y -direction. Cotter and Holm (2013) used the variational structure to propose other vertical slice Eady models, including a compressible model. This zoo was extended to anelastic and pseudocompressible Eady models in Cotter and Holm (2014). When moving away from a linear equation of state, models in this framework are not a reduction of a 3D counterpart, and they serve only to emulate an Eady flow configuration in the vertical slice setting for the purpose of evaluating numerical models. In the present work, we investigated the compressible vertical slice Eady model from this framework. It was hoped that the energy and

potential vorticity conservation would enable sustained baroclinic instability until frontogenesis, and we have indeed found this to be the case. We have made one minor modification to the model proposed by Cotter and Holm (2013), adding a constant perturbation Π_0 to the Exner pressure to reduce the vertical mean horizontal flow, making the setup more suitable for a numerical test problem.

The equations are

$$\frac{\partial \mathbf{u}}{\partial t} + (\mathbf{u} \cdot \nabla) \mathbf{u} - f v \hat{\mathbf{x}} = -c_p \theta_S \nabla \Pi - g \hat{\mathbf{z}}, \quad (1)$$

$$\frac{\partial v}{\partial t} + (\mathbf{u} \cdot \nabla) v + f u = \underbrace{c_p s (\Pi - \Pi_0)}_{\text{extra}}, \quad (2)$$

$$\frac{\partial \theta_S}{\partial t} + (\mathbf{u} \cdot \nabla) \theta_S = \underbrace{-v s}_{\text{extra}}, \quad (3)$$

$$\frac{\partial D}{\partial t} + \nabla \cdot (D \mathbf{u}) = 0, \quad (4)$$

where $\mathbf{u} = (u, w)$ is the velocity vector in the vertical slice, $\nabla = (\partial_x, \partial_z)$ is the gradient operator in the vertical slice, v is the out-of-slice velocity component, $\hat{\mathbf{x}}$ is a unit vector in the x -direction, and $\hat{\mathbf{z}}$ is that in the z -direction; D is the density, θ is the potential temperature, f is the rotation frequency, g is the acceleration due to gravity, and θ_S is a ‘‘perturbation potential temperature’’, with the idea that the total potential temperature $\theta \approx sy + \theta_S$ in the region near $y = 0$ where the slice model is defined, and for scaling purposes we write

$$s = -\frac{\theta_0 f \Lambda}{g} = \text{const.}, \quad (5)$$

where θ_0 is a reference density at the surface, and Λ is the constant vertical shear. Further, the Exner pressure Π depends on θ_S and D such that

$$\Pi = \left(\frac{p}{p_0} \right)^{R/c_p}, \quad p = DR \underbrace{T}_{=\theta_S \Pi}, \quad (6)$$

where p is the pressure, p_0 is a reference pressure, $R = c_p - c_v$ is the specific gas constant, c_p is the specific heat at constant pressure, and c_v is the specific heat at constant volume. All the variables \mathbf{u} , v , θ_S , D and Π depend on (x, z, t) only, hence the model can be solved on a 2D mesh.

It is important to note here that it is not physically correct to have Π depending on θ_S rather than θ , but this modification is necessary to have a well-defined vertical slice model. This model is not intended to skillfully predict physical phenomena, but rather to provide a challenging test case for atmosphere model numerics in a 2D configuration. This configuration can also be obtained by setting periodic boundary conditions to a 3D model (in local area model mesh configuration) in the y -direction and then making the mesh only 1 element wide (which is what we did in this paper). This is then testing the same code that is used in the 3D model, which is useful for verification purposes; it is also potentially more achievable in a code framework that does not easily switch between 3D and 2D. After this is done, the only other required changes to a 3D model are to insert the terms indicated as ‘‘extra’’ in Equations (1-4), having identified θ in the 3D model with θ_S in the vertical slice model.

The vertical slice model has steady state solutions when θ_S depends on z only, with $v = 0$, Π obtained from the hydrostatic balance,

$$0 = -c_p \theta_S \frac{\partial \Pi}{\partial z} - g, \quad (7)$$

and u obtained from the geostrophic balance,

$$f u = c_p s (\Pi - \Pi_0). \quad (8)$$

This solution can only be sustained with periodic boundary conditions in the x -direction. Here we see the role of Π_0 : without it, the vertical mean of u will be large and everything is propagating rapidly to the right.

This modification has a conserved total energy $E = K_u + K_v + P$, given by

$$K_u = \frac{1}{2} \int_{\Omega} D|\mathbf{u}|^2 dx dz, \quad (9)$$

$$K_v = \frac{1}{2} \int_{\Omega} Dv^2 dx dz, \quad (10)$$

$$P = \int_{\Omega} D(gz + c_v\Pi\theta - c_p\Pi_0\theta) dx dz, \quad (11)$$

where K_u is the kinetic energy from the in-slice velocity components, K_v is the kinetic energy from the out-of-slice velocity component, and P is the potential energy comprising contributions from gravitational potential energy and internal energy. For further discussion of the energy conservation and potential vorticity, see the Appendix.

2.2 Experimental settings

2.2.1 Constants

In the frontogenesis experiments, the model constants are set to the values below, following the incompressible Euler–Boussinesq Eady test case (e.g. Nakamura, 1994; Cullen, 2007; Visram et al., 2014; Visram, 2014; Yamazaki et al., 2017),

$$\begin{aligned} L &= 1000 \text{ km}, H = 10 \text{ km}, f = 10^{-4} \text{ s}^{-1}, \\ g &= 10 \text{ m s}^{-2}, p_0 = 10^5 \text{ Pa}, \theta_0 = 300 \text{ K}, \\ \Lambda &= 10^{-3} \text{ s}^{-1}, N^2 = 2.5 \times 10^{-5} \text{ s}^{-1}, \\ \Pi_0 &= 0.864, \end{aligned} \quad (12)$$

where L and H determine the model domain $\Omega = [-L, L] \times [0, H]$, and N is the Brunt-Väisälä frequency. The y derivative, s , of the background temperature in (3) and (2) is therefore calculated as

$$s = -\frac{\theta_0 f \Lambda}{g} = -3.0 \times 10^{-6}. \quad (13)$$

The Rossby and Froude numbers are given in the model as

$$\text{Ro} = \frac{u_0}{fL} = 0.05, \quad (14)$$

$$\text{Fr} = \frac{u_0}{NH} = 0.1, \quad (15)$$

where $u_0 = 5 \text{ m s}^{-1}$ is used as a representative velocity. The ratio of Rossby number to the Froude number defines the Burger number,

$$\text{Bu} = \text{Ro}/\text{Fr} = 0.5, \quad (16)$$

which is used in the next section for initialising the model.

2.2.2 Initialisation

The model field is initialised with a small perturbation to a balanced steady state. The steady state temperature is isothermal,

$$\bar{\theta}(z) = \theta_0 \exp(N^2(z - H/2)/g). \quad (17)$$

Then, following the incompressible Euler–Boussinesq Eady test case (e.g. Nakamura, 1994; Cullen, 2007; Visram et al., 2014; Yamazaki et al., 2017), a small perturbation is applied to the in-slice temperature,

$$\theta_S(x, z) = \bar{\theta} + \frac{\theta_0 a N}{g} \left\{ - \left[1 - \frac{\text{Bu}}{2} \coth \left(\frac{\text{Bu}}{2} \right) \right] \sinh Z \cos \left(\frac{\pi x}{L} \right) - n \text{Bu} \cosh Z \sin \left(\frac{\pi x}{L} \right) \right\}, \quad (18)$$

which is the structure of the normal mode taken from Williams (1967). The constant a corresponds to the amplitude of the perturbation, and the constant n takes the form of

$$n = \frac{1}{\text{Bu}} \left\{ \left[\frac{\text{Bu}}{2} - \tanh \left(\frac{\text{Bu}}{2} \right) \right] \left[\coth \left(\frac{\text{Bu}}{2} \right) - \frac{\text{Bu}}{2} \right] \right\}^{\frac{1}{2}}. \quad (19)$$

The modified vertical coordinate Z is defined as

$$Z = \text{Bu} \left[\left(\frac{z}{H} \right) - \frac{1}{2} \right]. \quad (20)$$

In fact, this is not a normal mode of the linearisation of the compressible vertical slice model. Instead, we rely upon initialising a balanced initial condition which will trigger a balanced baroclinically unstable mode. This is why our experiment has an initial growth period before resetting the clock to 0 when the amplitude starts to become visible.

Next we initialise the density D . Given the initial temperature θ_S in (18), first we seek Π in hydrostatic balance,

$$c_p \theta_S \frac{\partial \Pi}{\partial z} = -g. \quad (21)$$

Once we have the profile of the initial Π , we can calculate the initial density by using (6) as

$$D = \frac{p_0 \Pi \frac{c_v}{R_d}}{R_d \theta_0}. \quad (22)$$

Alternatively, we can solve the nonlinear problem of finding D such that (21) holds, treating Π as the prescribed function of D and θ_S given in (6). This is what we did in our experiments (see Cotter and Shipton (2023) for details).

Then we initialize the out-of-slice velocity v by seeking a velocity in geostrophic balance with the initialised θ_S and Π :

$$-fv = -c_p \theta_S \frac{\partial \Pi}{\partial x}. \quad (23)$$

Finally, we initialise the in-slice velocity u according to

$$u = \frac{c_p}{f} \frac{\partial \bar{\theta}}{\partial y} (\Pi - \Pi_0). \quad (24)$$

Here Π_0 was chosen following numerical experiments to minimise the horizontal drift of the front structures once they have formed.

In addition to the initialisation of the model field described above, we introduce a breeding procedure at the beginning of each simulation to remove any remaining unbalanced modes in the initial condition,

as in Visram et al. (2014); Visram (2014); Yamazaki et al. (2017). In the experiments performed in section 3, the model field is initialised with a small perturbation by choosing $a = -7.5$ in (18), following the previous studies. The simulation is then advanced until the maximum amplitude of v reaches 3 m s^{-1} , at which point the time is reset to zero to match the amplitude of the initial perturbation with that of the incompressible Euler–Boussinesq Eady models (Nakamura and Held, 1989; Visram et al., 2014; Yamazaki et al., 2017) as closely as possible. In the results presented in Section 3, the time is reset to zero after 50 hours, both with the default resolution and with the high resolution.

3 Results

In this section, we present the results of the frontogenesis experiments using the new test case developed in this study, with the use of the finite element code generation library Firedrake (Ham et al., 2023). Since this paper is about the testcase and not the specific numerical discretisation, we just briefly mention that we used a compatible finite element discretisation following Cotter and Shipton (2023) in 3D configuration on a mesh that is one cell wide and periodic in the y -direction, with just two differences. First, we did not use the edge stabilisation recommended there for θ_S transport as it led to instabilities after the front formed, requiring further investigation. It appears that the horizontal discontinuous Galerkin upwinding for θ_S is sufficient for this problem, probably because the curvature of the solution is mainly in the horizontal direction. Second, we did not use a vector invariant form of the velocity advection equation, instead using a discretisation of the standard advective form $(\mathbf{u} \cdot \nabla)\mathbf{u}$ in our main results, using the upwind formulation of Cockburn et al. (2007) for that term instead. This is discussed more later. The timestepping method is the implicit midpoint rule, which is solved using Newton’s method and GMRES preconditioned by the column patch additive Schwarz method, which is also described in Cotter and Shipton (2023). This scheme is unconditionally stable and preserves energy for linear wave equations; any dissipation in the model is coming from upwinding in the spatial discretisation.

The constants used to set up the experiments are shown in section 2.2.1. At the beginning of each experiment, the model is initialised in the way described in section 2.2.2, then integrated for 25 days in each experiment.

In our solution, the model resolution is given by

$$\Delta x = \frac{2L}{N_x}, \quad \Delta z = \frac{H}{N_z}, \quad (25)$$

where N_x and N_z are the number of quadrilateral elements in the x - and z -directions, respectively. Unless stated otherwise, we use a resolution of $N_x = 30$ and $N_z = 30$, and the time step Δt of 300 s.

Figures 1 and 2 show the snapshots of the out-of-slice velocity v and potential temperature θ fields, respectively. At day 2, both fields show very similar structures to those from the simulation using the linearised equations in Visram (2014). The model shows some early signs of front formation at day 4. The frontal discontinuity becomes most intense around day 7. At day 11, the vertical tilt in the v -field reverses, which is a sign of energy conversion from kinetic back to potential energy. Overall, these results are consistent with the incompressible Eady models (Nakamura and Held, 1989; Cullen, 2007; Visram et al., 2014; Visram, 2014; Yamazaki et al., 2017). The black curve in Figure 3 shows the time evolution of the root mean square of v (RMSV) in our model. The result shows that the model reproduces several further quasi-periodic lifecycles after the first frontogenesis.

To evaluate the effect of resolution on our model result, we repeated the experiment using $N_x = 60$ in stead of $N_x = 30$. A time step of $\Delta t = 120$ s is used for the high-resolution run. The number of layers is kept at $N_z = 30$. The evolution of RMSV in the high-resolution run is shown by the red curve in Figure 3. It shows front cycles with bigger RMSV at the peaks compared the the low-resolution results.

Figure 4 shows the time evolution of the total energy E , the kinetic energy K_u and K_v , and the potential energy P , which are defined by the equations (9) to (11). We observe a loss of energy after

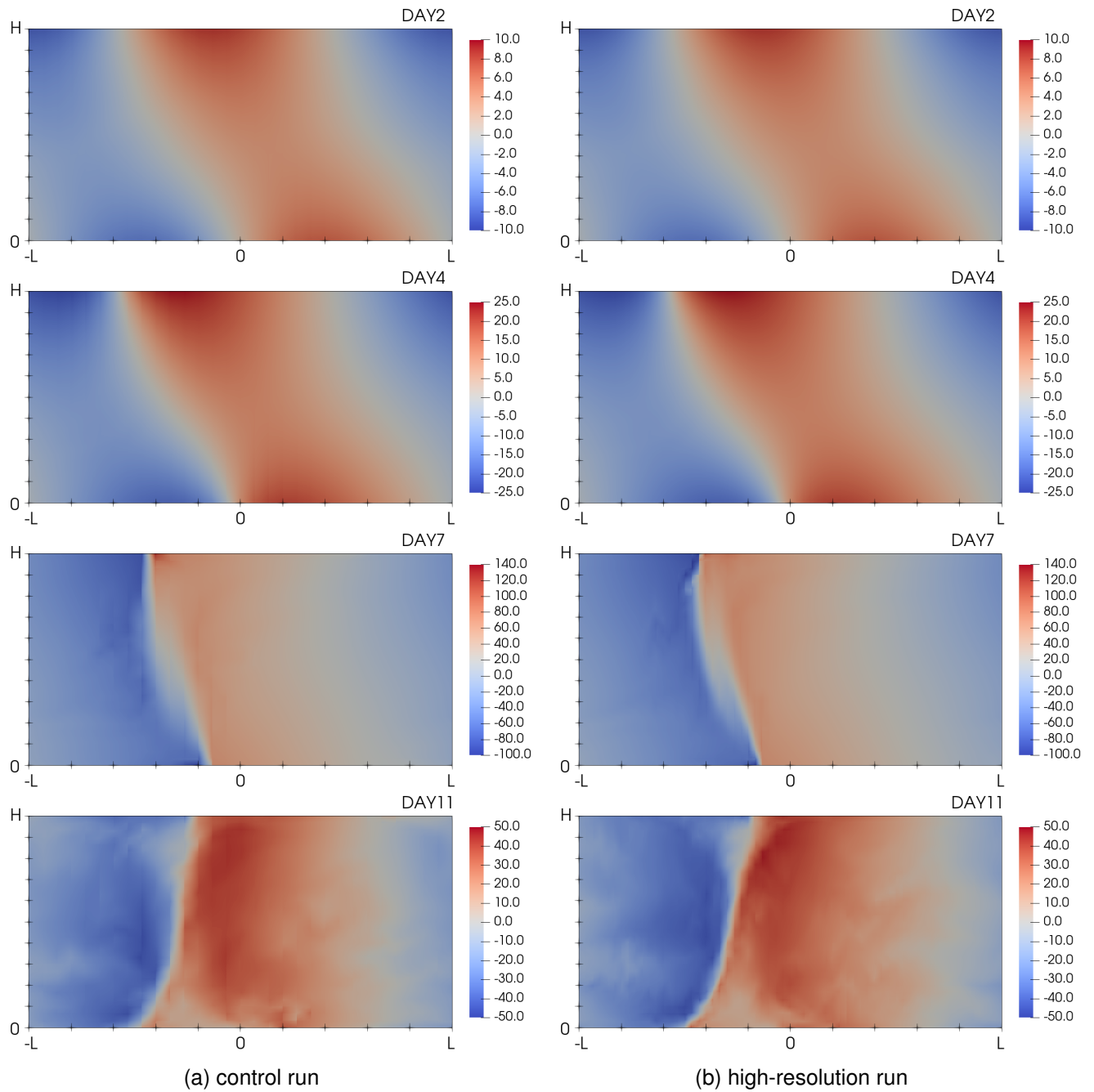


Figure 1: Snapshots of out-of-slice velocity fields at days 2, 4, 7, and 11 in (a) the control run and (b) the high-resolution run.

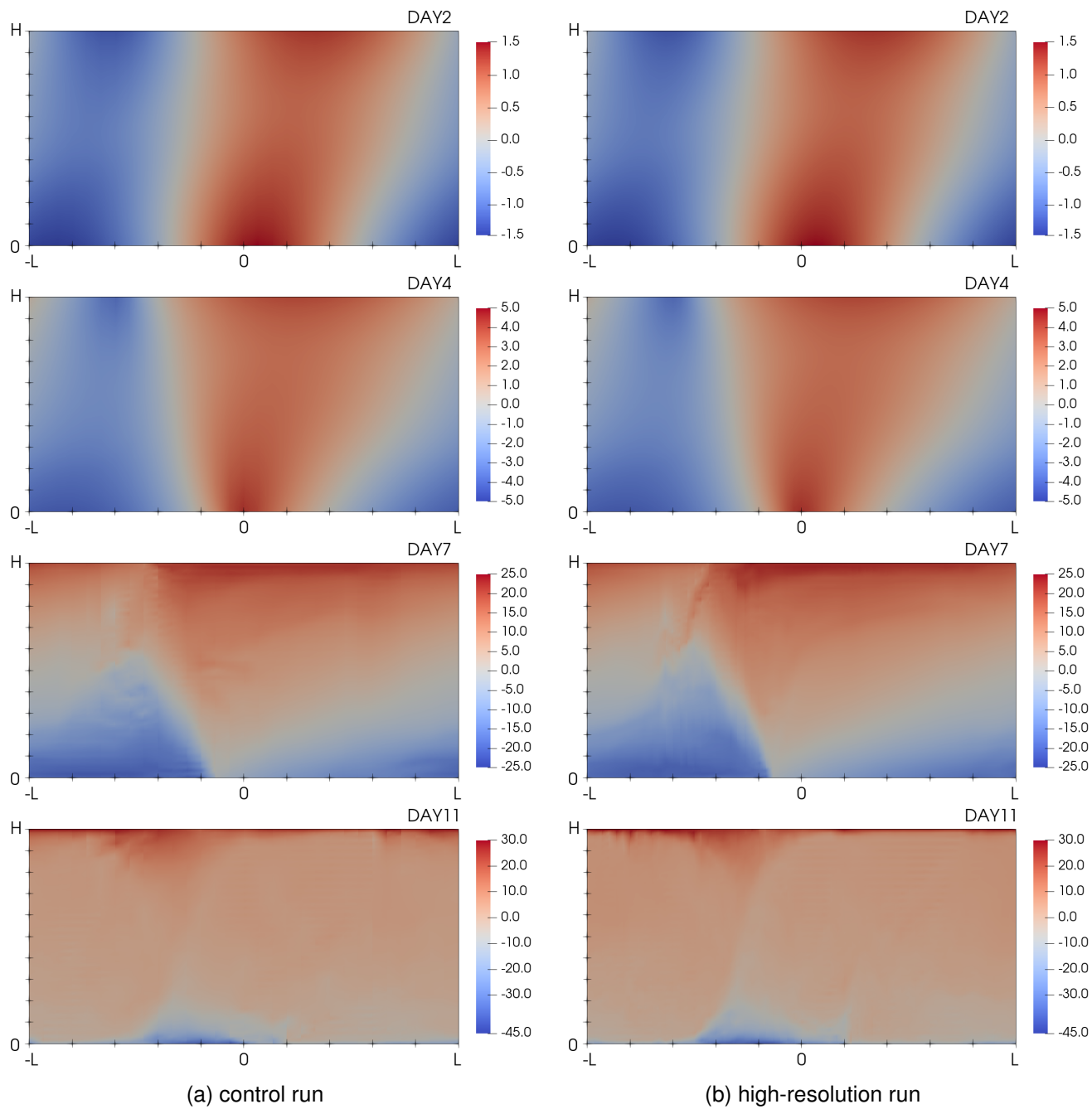


Figure 2: Snapshots of in-slice temperature perturbation field at days 2, 4, 7, and 11 in (a) the control run and (b) the high-resolution run.

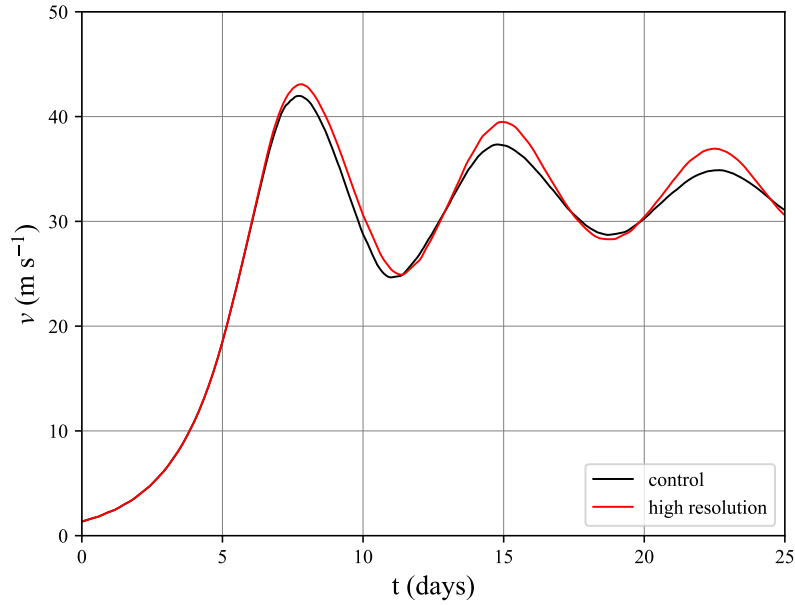


Figure 3: The root mean square of the out-of-slice velocity in the control run (black) and in the high-resolution run (red).

the front is formed, which is due to loss of available potential energy caused by numerical dissipation in the θ_S equation as well as loss of K_v due to numerical dissipation in the v equation. This demonstrates the challenge posed by fronts in atmosphere models; numerical dissipation is necessary to stabilise advection in the model but is also altering the large scale circulation.

Finally, as an example of how the testcase might be used to compare numerical schemes, we replace the advection term $(\mathbf{u} \cdot \nabla)\mathbf{u}$ in the velocity equation with the vector invariant form $(\nabla \times \mathbf{u}) \times \mathbf{u} + |\mathbf{u}|^2/2$, using the upwind discretisation of Cotter and Shipton (2023). As shown in Figure 5, by day 6 the version using the vector invariant form has developed oscillations that are polluting the solution. We believe that this is related to the ‘‘Hollingsworth instability’’ which is much discussed in the dynamical core literature (Hollingsworth et al., 1983; Lazić et al., 1984; Gassmann, 2013; Bell et al., 2017; Peixoto et al., 2018). This example requires further investigation, but might provide a useful laboratory to further understanding how to control that instability.

4 Conclusion

A new vertical slice test case is developed for compressible nonhydrostatic dynamical cores of atmospheric models, and solutions of a model using an implicit time-stepping method and a compatible finite element method were presented as a reference. The test case can be easily run by adding two terms to a 3D atmosphere model in local area mode, i.e. a Cartesian box, with periodicity and being one cell wide in the y -direction. It provides the capability to explore the behaviour of discretisations in the presence of challenging fronts but in a quasi-2D configuration that allows rapid turnaround for numerical experiments. The equations for the test case do not correspond to the reduction of a 3D model to a 2D vertical slice configuration, since this is not possible for a compressible model with nonlinear equation of state. However, it serves our purpose since we observe solutions that produce features characteristic of atmospheric fronts, which we would like to challenge our numerical schemes with.

We demonstrated that the test case produces quasi-periodic lifecycles of fronts which are observed

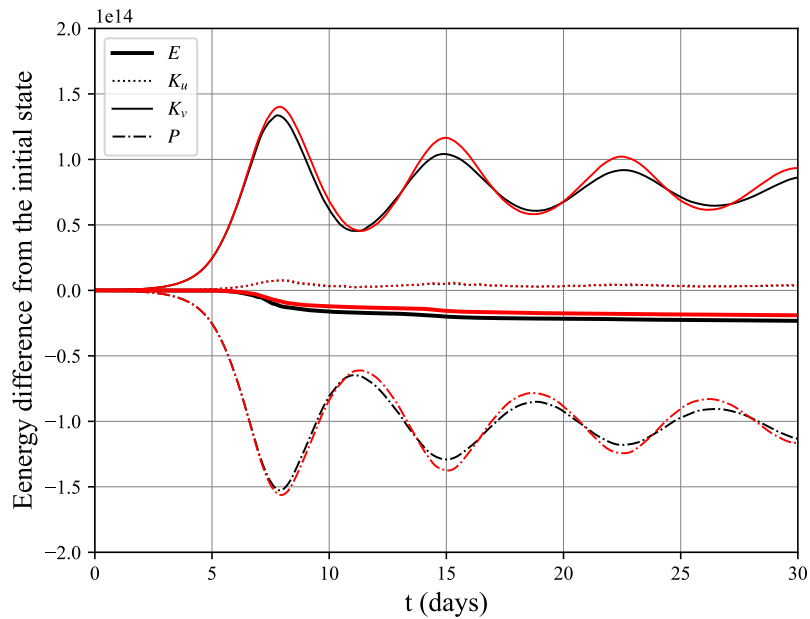


Figure 4: Time evolution of energy in the control run (black) and in the high-resolution run (red). Thick line represents the evolution of total energy. Dotted and solid lines represent the evolutions of in-slice and out-of-slice components of the kinetic energy. Dot-dashed line represents the evolution of potential energy.

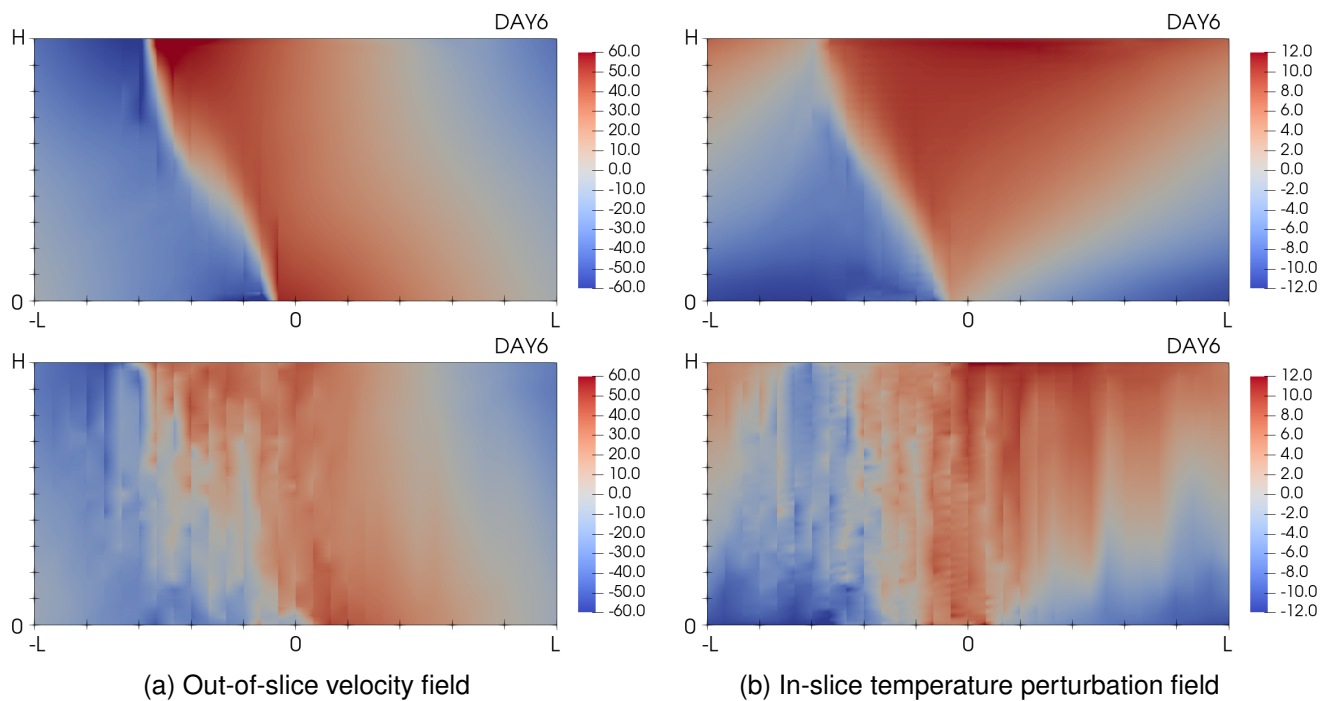


Figure 5: Snapshots of out-of-slice velocity and in-slice temperature perturbation at day 6. top: advective form, bottom: vector invariant form.

despite the presence of strong discontinuities; these are sustained because the equations have conserved energy and potential vorticity. Without this formulation, solutions are insufficiently constrained to drive strong fronts, as was observed by Cullen (2008). The general results of frontogenesis are consistent with results from the incompressible Euler–Boussinesq models, so we have been successful in our goals for the test case.

We hope that this test case becomes adopted by atmosphere modelling groups, allowing intercomparisons of different discretisations and approaches. One possible use for the test case is to understand how subgrid schemes, both explicit and implicit, behave in the region of fronts. For example, the compressible version of the α -Euler vertical slice model of Cotter and Holm (2013) could be used for this. In addition, the test case could be extended to include the effects of moisture, and boundary layer physics, for example.

To complete the programme of Cullen (2007) in this setting, it remains to prove rigorously that the solution of our compressible vertical slice model converges in the semigeostrophic limit to solutions of their semigeostrophic counterpart, following an adaptation of Cullen and Maroofi (2003) to include the extra terms marked in ((1)-4). This analysis can also be used to obtain a semigeostrophic reference solution, following the approaches of Egan et al. (2022); Benamou et al. (2024). We leave this mathematical analysis to future work.

Acknowledgement We are grateful for funding from EPSRC via grant EP/R029628/1, and from NERC via grant NE/K012533/1. We would like to thank Thomas Bendall, Mike Cullen, Darryl Holm and Jemma Shipton for their helpful comments on our paper. Any errors are the author’s own.

References

- Bell, M.J., Peixoto, P.S., Thuburn, J., 2017. Numerical instabilities of vector-invariant momentum equations on rectangular C-grids. *Quarterly Journal of the Royal Meteorological Society* 143, 563–581.
- Benamou, J.D., Cotter, C.J., Malamut, H., 2024. Entropic optimal transport solutions of the semi-geostrophic equations. *Journal of Computational Physics* 500, 112745.
- Cockburn, B., Kanschat, G., Schötzau, D., 2007. A note on discontinuous Galerkin divergence-free solutions of the Navier–Stokes equations. *Journal of Scientific Computing* 31, 61–73.
- Cotter, C., Holm, D., 2013. A variational formulation of vertical slice models. *Proceedings of the Royal Society of London A: Mathematical, Physical and Engineering Sciences* 469, 20120678.
- Cotter, C., Holm, D., 2014. Variational formulations of sound-proof models. *Quarterly Journal of the Royal Meteorological Society* 140, 1966–1973.
- Cotter, C.J., Cullen, M., 2019. Particle relabelling symmetries and Noether’s theorem for vertical slice models. *Journal of Geometric Mechanics* 11, 139–151.
- Cotter, C.J., Shipton, J., 2023. A compatible finite element discretisation for the nonhydrostatic vertical slice equations. *GEM-International Journal on Geomathematics* 14, 25.
- Cullen, M., 2007. Modelling atmospheric flows. *Acta Numerica* 16, 67–154.
- Cullen, M., 2008. A comparison of numerical solutions to the Eady frontogenesis problem. *Quarterly Journal of the Royal Meteorological Society: A journal of the atmospheric sciences, applied meteorology and physical oceanography* 134, 2143–2155.

- Cullen, M., Maroofi, H., 2003. The fully compressible semi-geostrophic system from meteorology. *Archive for rational mechanics and analysis* 167, 309–336.
- Cullen, M.J., 2006. A mathematical theory of large-scale atmosphere/ocean flow. Imperial College Press.
- Egan, C.P., Bourne, D.P., Cotter, C.J., Cullen, M.J., Pelloni, B., Roper, S.M., Wilkinson, M., 2022. A new implementation of the geometric method for solving the Eady slice equations. *Journal of Computational Physics* 469, 111542.
- Galewsky, J., Scott, R.K., Polvani, L.M., 2004. An initial-value problem for testing numerical models of the global shallow-water equations. *Tellus A: Dynamic Meteorology and Oceanography* 56, 429–440.
- Gassmann, A., 2013. A global hexagonal C-grid non-hydrostatic dynamical core (ICON-IAP) designed for energetic consistency. *Quarterly Journal of the Royal Meteorological Society* 139, 152–175.
- Hall, D.M., Ullrich, P.A., Reed, K.A., Jablonowski, C., Nair, R.D., Tufo, H.M., 2016. Dynamical Core Model Intercomparison Project (DCMIP) tracer transport test results for CAM-SE. *Quarterly Journal of the Royal Meteorological Society* 142, 1672–1684.
- Ham, D.A., Kelly, P.H.J., Mitchell, L., Cotter, C.J., Kirby, R.C., Sagiyama, K., Bouziani, N., Vorderwuelbecke, S., Gregory, T.J., Betteridge, J., Shapero, D.R., Nixon-Hill, R.W., Ward, C.J., Farrell, P.E., Brubeck, P.D., Marsden, I., Gibson, T.H., Homolya, M., Sun, T., McRae, A.T.T., Luporini, F., Gregory, A., Lange, M., Funke, S.W., Rathgeber, F., Bercea, G.T., Markall, G.R., 2023. *Firedrake User Manual*. first edition ed. Imperial College London and University of Oxford and Baylor University and University of Washington. doi:10.25561/104839.
- Hollingsworth, A., Kållberg, P., Renner, V., Burridge, D., 1983. An internal symmetric computational instability. *Quarterly Journal of the Royal Meteorological Society* 109, 417–428.
- Läuter, M., Handorf, D., Dethloff, K., 2005. Unsteady analytical solutions of the spherical shallow water equations. *Journal of computational physics* 210, 535–553.
- Lavier, T., 2024. A semi-discrete optimal transport scheme for the 3d incompressible semi-geostrophic equations. arXiv preprint arXiv:2411.00575 .
- Lazić, L., Janjić, Z., Mesinger, F., 1984. “non-cancellation” instability in horizontal advection schemes for momentum equations. *Meteorology and Atmospheric Physics* 35, 49–52.
- Nakamura, N., 1994. Nonlinear equilibration of two-dimensional Eady waves: Simulations with viscous geostrophic momentum equations. *Journal of the Atmospheric Sciences* 51, 1023–1035.
- Nakamura, N., Held, I.M., 1989. Nonlinear equilibration of two-dimensional Eady waves. *Journal of the Atmospheric Sciences* 46, 3055–3064.
- Peixoto, P.S., Thuburn, J., Bell, M.J., 2018. Numerical instabilities of spherical shallow-water models considering small equivalent depths. *Quarterly Journal of the Royal Meteorological Society* 144, 156–171.
- Ullrich, P., Reed, K., Jablonowski, C., 2015. Analytical initial conditions and an analysis of baroclinic instability waves in f - and β -plane 3D channel models. *Quarterly Journal of the Royal Meteorological Society* 141, 2972–2988.
- Ullrich, P.A., Jablonowski, C., Kent, J., Lauritzen, P.H., Nair, R., Reed, K.A., Zarzycki, C.M., Hall, D.M., Dazlich, D., Heikes, R., et al., 2017. DCMIP2016: a review of non-hydrostatic dynamical core design and intercomparison of participating models. *Geoscientific Model Development* 10, 4477–4509.

- Ullrich, P.A., Jablonowski, C., Kent, J., Lauritzen, P.H., Nair, R.D., Taylor, M.A., 2012. Dynamical core model intercomparison project (DCMIP) test case document. DCMIP Summer School 83.
- Visram, A., 2014. Asymptotic limit analysis for numerical models of atmospheric frontogenesis. PhD thesis, Imperial College London , 238.
- Visram, A., Cotter, C., Cullen, M., 2014. A framework for evaluating model error using asymptotic convergence in the Eady model. Quarterly Journal of the Royal Meteorological Society 140, 1629–1639.
- Williams, R., 1967. Atmospheric frontogenesis: A numerical experiment. Journal of the Atmospheric Sciences 24, 627–641.
- Williamson, D.L., Drake, J.B., Hack, J.J., Jakob, R., Swarztrauber, P.N., 1992. A standard test set for numerical approximations to the shallow water equations in spherical geometry. Journal of computational physics 102, 211–224.
- Yamazaki, H., Shipton, J., Cullen, M.J., Mitchell, L., Cotter, C.J., 2017. Vertical slice modelling of non-linear eady waves using a compatible finite element method. Journal of Computational Physics 343, 130–149.
- Zarzycki, C.M., Jablonowski, C., Kent, J., Lauritzen, P.H., Nair, R., Reed, K.A., Ullrich, P.A., Hall, D.M., Taylor, M.A., Dazlich, D., et al., 2019. DCMIP2016: the splitting supercell test case. Geoscientific Model Development 12, 879–892.

A Variational derivation of the model

In this appendix we briefly summarise the variational derivation of the vertical slice compressible Eady model, since it slightly differs from the model presented in Section 5 of Cotter and Holm (2013), due to the modification to the Exner pressure. The Lagrangian for the system is

$$\ell[\mathbf{u}, v, D, \theta_S] = \int_{\Omega} \underbrace{\frac{D}{2} (|\mathbf{u}|^2 + v^2) + f D v x}_{\text{total kinetic energy}} - \underbrace{g D z}_{\text{gravitational potential energy}} - \underbrace{D \theta_S (c_v \Pi - c_p \Pi_0)}_{\text{internal energy}} dx dz, \quad (26)$$

where θ_S is the in-slice temperature, transported according to

$$\frac{\partial \theta_S}{\partial t} + \mathbf{u} \cdot \nabla \theta_S + s v = 0, \quad (27)$$

with the idea that the total potential temperature is $\theta \approx \theta_S + s y$ in the region of $y = 0$, where D is the in-slice density, transported according to

$$\frac{\partial D}{\partial t} + \nabla \cdot (\mathbf{u} D) = 0. \quad (28)$$

(26) differs from the Lagrangian in Cotter and Holm (2013) by the inclusion of Π_0 , a constant. Combining the two formulae in (6) gives

$$\Pi = \left(\frac{D R \theta_S}{p_0} \right)^{\gamma-1}, \quad (29)$$

where $\gamma = c_p/c_v$, and we have

$$\frac{\partial \Pi}{\partial \theta_S} = \frac{\gamma-1}{\theta_S} \Pi = \frac{R}{c_v \theta_S} \Pi, \quad \frac{\partial \Pi}{\partial D} = \frac{R}{c_v D} \Pi. \quad (30)$$

The functional derivatives are then

$$\frac{\delta \ell}{\delta \mathbf{u}_S} = D\mathbf{u}_S, \quad (31)$$

$$\frac{\delta \ell}{\delta v} = D(v + fx), \quad (32)$$

$$\frac{\delta \ell}{\delta D} = \frac{1}{2}(\|\mathbf{u}\|^2 + v^2) + fvx - gz - c_p\theta_S(\Pi - \Pi_0), \quad (33)$$

$$\frac{\delta \ell}{\delta \theta_S} = c_p D(\Pi - \Pi_0). \quad (34)$$

Substitution into Equations 2.9 of Cotter and Holm (2013) then gives

$$\begin{aligned} \frac{\partial D\mathbf{u}}{\partial t} + \nabla \cdot (\mathbf{u} \otimes D\mathbf{u}) + (\nabla \mathbf{u})^T \cdot D\mathbf{u} + D(v + fx)\nabla v \\ - D\nabla \left(\frac{1}{2}(\|\mathbf{u}\|^2 + v^2) + fvx - gz - c_p\theta_S(\Pi - \Pi_0) \right) + c_p D(\Pi - \Pi_0)\nabla \theta_S = 0, \end{aligned} \quad (35)$$

$$\frac{\partial D(v + fx)}{\partial t} + \nabla \cdot (\mathbf{u}D(v + fx)) + sc_p D(\Pi - \Pi_0) = 0, \quad (36)$$

and further manipulations in combination with Equations (27) and (28) lead to Equations (1-4), noting that $\nabla \Pi_0 = 0$ (because Π_0 is a constant).

Appendix B of Cotter and Holm (2013) derives the Lie-Poisson formulation for the vertical slice framework, demonstrating a conserved energy/Hamiltonian given by

$$E = \int_{\Omega} \frac{\delta \ell}{\delta \mathbf{u}} \cdot \mathbf{u} + \frac{\delta \ell}{\delta v} v \, dx \, dz - \ell[\mathbf{u}, v, \theta_S, D]. \quad (37)$$

For ℓ from (26), this becomes

$$E = \int_{\Omega} \frac{D}{2} (|\mathbf{u}|^2 + v^2) + gDz + D\theta_S(c_v\Pi - c_p\Pi_0) \, dx \, dz, \quad (38)$$

which just corresponds to the (relative, i.e. the Coriolis part is removed) kinetic energy plus the potential energy, as expected.

Finally, from Equation 2.11 of Cotter and Holm (2013) we have the vertical slice Kelvin circulation theorem,

$$\frac{d}{dt} \oint_{C(t)} \left(s \frac{1}{D} \frac{\delta \ell}{\delta \mathbf{u}} - \frac{1}{D} \frac{\delta \ell}{\delta v} \nabla \theta_S \right) \cdot d(x, z) = 0, \quad (39)$$

where $C(t)$ is a closed loop transported in the x - z plane by the in-slice velocity \mathbf{u} . For ℓ from (26), this becomes

$$\frac{d}{dt} \oint_{C(t)} (s\mathbf{u} - (v + fx)\nabla \theta_S) \cdot d(x, z) = 0. \quad (40)$$

After application of Stokes' Theorem and consideration of arbitrary $C(t)$, we obtain the material conservation of potential vorticity q ,

$$\frac{\partial q}{\partial t} + \mathbf{u} \cdot \nabla q = 0, \quad q = (s \operatorname{curl} \mathbf{u} + \nabla \theta_S \times (\nabla v + f\hat{x})) \cdot \hat{y} \, d(x, z), \quad (41)$$

where \hat{x} and \hat{y} are the unit vectors pointing in the x - and y - directions respectively.